Chemical Science

ROYAL SOCIETY OF CHEMISTRY

EDGE ARTICLE

View Article Online
View Journal | View Issue

Check for updates

Cite this: *Chem. Sci.*, 2025, **16**, 9720

All publication charges for this article have been paid for by the Royal Society of Chemistry

Received 8th March 2025
Accepted 20th April 2025

DOI: 10.1039/d5sc01852h

rsc.li/chemical-science

Open Access Article. Published on 21 April 2025. Downloaded on 2/20/2026 6:43:14 PM. This article is licensed under a Creative Commons Attribution-NonCommercial 3.0 Unported Licence.

Aptamer single-molecule dispersion on single-atom anchoring sites for high-selectivity *in vivo* detection†

Jing Huang, Shiting Gu, Xue Zhou, Yibin Liu and Zhonghai Zhang *

Traditional aptasensors struggle to distinguish molecules with highly similar chemical structures due to the inherent flexibility of aptamers, which form 'nano-bushes' causing non-specific adsorption and reducing sensor specificity. To address this, we propose a novel strategy of anchoring aptamers at the single-molecule level onto atomic anchoring sites. We have designed a gold single-atom/titanium dioxide (Au SA/TiO_2) photoelectrode to immobilize a dopamine (DA)-selective aptamer, enabling the fabrication of a photoelectrochemical single-molecule aptamer sensor (PEC-sm-aptasensor). This sensor can selectively detect DA *in vivo* in different brain regions of living mice. This advancement has revolutionized our understanding of DA variation in the prefrontal cortex of Parkinson's disease (PD) mice. In contrast to previous beliefs, we have discovered a new neurotransmitter dynamic pattern: while the total concentration of neurotransmitters decreases, the concentration of DA remains constant, thus not affecting cognitive levels. This finding is crucial for a more targeted understanding of PD and opens avenues for more effective treatments and diagnostic methods.

Introduction

Molecular recognition units are essential for the specificity of biosensors. Unlike traditional biorecognition elements such as enzymes and antibodies, which are derived from living organisms, aptamers are unique functional nucleic acids that can be artificially synthesized. They are created through a process known as Systematic Evolution of Ligands by Exponential Enrichment (SELEX), offering a versatile and adaptable alternative for biosensor development.[1–3] Aptamers achieve target binding through non-covalent interactions such as van der Waals forces and hydrogen bonds, which confer unique spatial conformations and result in exceptional stability and customizable selectivity.[4,5] Through successful screening, numerous aptamers have been integrated into diverse biosensor designs, contributing to the advancement and broad application of biosensing technologies. In particular, electrochemical aptasensors have gained significant acclaim for their high sensitivity, swift response times, and compatibility with portable device integration, making them highly effective for a wide array of detection applications.[6–9] Kevin Plaxco and Netzahualcoyotl Arroyo-Curras have pioneered aptamer-based electronic sensors (E-AB sensors), advancing aptasensor technology by integrating target molecule recognition with signal transduction, thereby enhancing real-world application efficiency.[10–14] Anne M. Andrews has made pivotal contributions to molecular detection by enabling receptor-functionalized field-effect transistor surfaces to bind with aptamers for signal detection in high ionic strength solutions and by developing neuro-probes for serotonin release determination in the brain.[15,16]

Despite significant progress, electrochemical aptasensors still encounter a substantial challenge in the selective identification of molecules with highly similar chemical structures. A prime example is the differentiation among monoamine neurotransmitters—dopamine (DA), norepinephrine (NE), epinephrine (EP), and 5-hydroxytryptamine (5-HT)—which are crucial for the nervous system's function and are implicated in various neurological disorders.[17,18] The subtle differences in their molecular structures make their discrimination a complex analytical task for conventional electrochemical aptasensors. The primary obstacle in achieving this selectivity lies in the post-SELEX adaptation of aptamers onto electrode surfaces. Aptamers are highly flexible single-stranded DNA or RNA molecules, which tend to form "nano-bushes" when immobilized on the electrode surface, leading to non-specific adsorption and a consequent reduction in sensor specificity. This issue undermines the ability of electrochemical aptasensors to accurately distinguish between closely related molecules, thus limiting their effectiveness in complex biological environments.[19] Beyond further optimization of aptamer sequences to enhance target selectivity,[20,21] future efforts should focus on immobilizing aptamers on substrates with a single-molecule

Shanghai Key Laboratory of Green Chemistry and Chemical Processes, School of Chemistry and Molecular Engineering, East China Normal University, Dongchuan Road 500, Shanghai 200241, China. E-mail: zhzhang@chem.ecnu.edu.cn

† Electronic supplementary information (ESI) available. See DOI: https://doi.org/10.1039/d5sc01852h

© 2025 The Author(s). Published by the Royal Society of Chemistry

Open Access Article. Published on 21 April 2025. Downloaded on 2/20/2026 6:43:14 PM. This article is licensed under a Creative Commons Attribution-NonCommercial 3.0 Unported Licence.

level distribution. Utilizing individual atoms as anchoring points is an ideal strategy for dispersing aptamers at this level, ensuring a more precise and effective detection mechanism.

Herein, we introduce an atomic-level dispersion anchoring strategy designed to bind aptamers at individual atomic sites, thereby facilitating a single-molecule level distribution of aptamers. This innovative approach is aimed at enhancing the selectivity and specificity of electrochemical aptasensors. To validate the advantages of our proposed strategy, we have embarked on a challenging endeavour: distinguishing DA from its structurally similar analogues, including NE, EP, and 5-HT, within the *in vivo* rodent brain environment. Despite the fact that detection methods based on metal–organic frameworks (MOFs), covalent organic frameworks (COFs), or fluorescence sensors have achieved good detection results for dopamine, DA,[22–25] photoelectrochemical (PEC) detection has not yet obtained very good selectivity. We have engineered TiO_2 with oxygen vacancies and decorated with gold single-atoms to fabricate the Au SA/TiO_2 photoelectrode. The single atomic sites ensure the secure immobilization of DA-selective monomolecular aptamers through the unique Au–S bond, enabling highly selective PEC sensing directly within the *in vivo* milieu. The preference for PEC detection modalities, as opposed to conventional electrochemical techniques, stems from their innate capacity to elicit analytical signals in the absence of extrinsic bias, an attribute of paramount importance for non-disruptive interrogation of neuronal circuits.[26,27] This methodology not only circumvents the potential for perturbing the endogenous electrophysiological milieu but also amplifies the fidelity and selectivity of detection, offering an unparalleled analytical scaffold for the precise delineation of neurochemical dynamics. The rationally designed PEC-single molecular aptamer sensor (PEC-sm-aptasensor) is implanted into different brain regions of living mice for long-term *in vivo* detection of DA. Leveraging the exceptional selectivity of the PEC-sm-aptasensor for DA, we have observed a novel pattern of neurotransmitter dynamics that starkly contrasts with previous conclusions. In Parkinson's disease (PD) models, it was traditionally believed that DA levels in the cortex decrease sharply.[28] Our assays have unveiled a significant reduction in the levels of monoamine neurotransmitters (DA, NE, EP, and 5-HT) in the cortex of the PD mice compared to that in normal rodents, while the concentration of DA remains essentially unchanged. This revelation is a direct consequence of enhanced capability to selectively identify DA in an *in vivo* milieu, which, in turn, serves as a compelling testament to the efficacy and utility of our strategic approach.

Results and discussion

The design and manufacture of the PEC-sm-aptasensor are detailed in the Experimental section in the ESI.† In brief, TiO_2 photoelectrodes were created *via* a two-step anodization process on thin Ti wire.[29] Au single-atoms (Au SA) were deposited on TiO_2 using cryo-electrochemical deposition, while Au nanoparticle–TiO_2 (Au NP/TiO_2) photoelectrodes were prepared by sputtering Au nanoparticles onto TiO_2. The DA aptamer (oligonucleotide sequences are in the Experimental section in the ESI†) binds to both Au SA/TiO_2 and Au NP/TiO_2 through Au–S linkages (Fig. S1 in the ESI†).

As shown in Fig. 1, traditional aptamer–Au NP/TiO_2 and novel aptamer–Au SA/TiO_2 photoelectrodes were compared for their specific recognition capabilities in selective *in vivo* PEC detection of DA in the brains of living mice. The Au NPs/TiO_2 photoelectrode allows multiple aptamers to connect on the Au NP surface, forming a nano-bush structure that increases non-specific binding and reduces selectivity. In contrast, the Au SA/TiO_2 photoelectrode has isolated gold atoms forming a single Au–S bond with one aptamer, preventing cross-linking and non-specific interactions, and ensuring high selectivity.

The micro-PEC-sm-aptasensor, fabricated on thin Ti wire with a conical structure (top diameter: 10 μm, Fig. 2a), enhances tissue implantation and reduces damage. SEM imaging (Fig. 2b) reveals patterned optical-nanostructures with highly ordered periodic top-nanoring, enabling effective photon localization and efficient near-infrared photon acquisition *in vivo* (optical absorption activity is illustrated in Fig. S2 in the ESI†). HRTEM imaging (Fig. 2c) shows well-resolved lattice fringes (interplanar distance: 0.346 nm) with slight disorder and dislocation at crystal edges, indicating oxygen vacancy-based defects.[30] EPR spectra (Fig. S3 in the ESI†) provide evidence of oxygen vacancies with a sharp signal at $g = 2.003$.[31]

AC HAADF-STEM imaging (Fig. 2d) identifies isolated bright spots (highlighted by red circles) as Au single-atoms (SAs) due to their high atomic weight. No Au clusters or nanoparticles were detected in the observation range or *via* X-ray diffraction (Fig. S4 in the ESI†). Line scan spectrogram analysis of the AC HAADF-STEM image (Fig. 2e) shows Ti and Au metallic atoms, with Au presenting higher contrast due to its atomic weight. A 3D colour heatmap (Fig. 2f) visually represents isolated Au atoms on the TiO_2 substrate.

XANES and EXAFS analyses further investigate the Au SA structure. XANES spectra (Fig. 2g) show higher white line intensity for Au SA/TiO_2 compared to Au foil, indicating a high valence state of Au. FT-EXAFS spectra (Fig. 2h) display a main peak at 1.57 Å (Au–O path) with no Au–Au coordination peaks (at 2.51 Å),[32] confirming atomic Au dispersion. The wavelet transform (WT) of EXAFS oscillations validates atomic Au dispersion, showing distinct intensity contributions for Au–Au (Au foil, Fig. 2i) and Au–O (Au SA sample, Fig. 2j). EXAFS fitting (Fig. S5 and Table S1 in the ESI†) reveals that each Au atom is coordinated with two O and two Ti atoms.

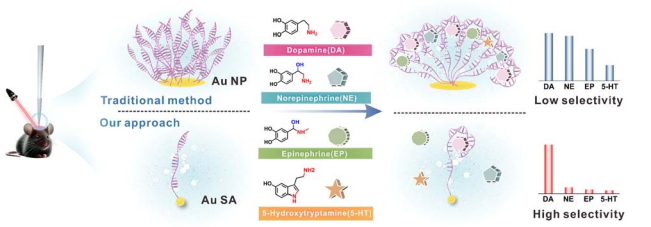

Fig. 1 Schematic illustration of DA aptamer bonded to Au NPs and Au SA for specific recognition of DA and other neurotransmitters.

Open Access Article. Published on 21 April 2025. Downloaded on 2/20/2026 6:43:14 PM.
This article is licensed under a Creative Commons Attribution-NonCommercial 3.0 Unported Licence.

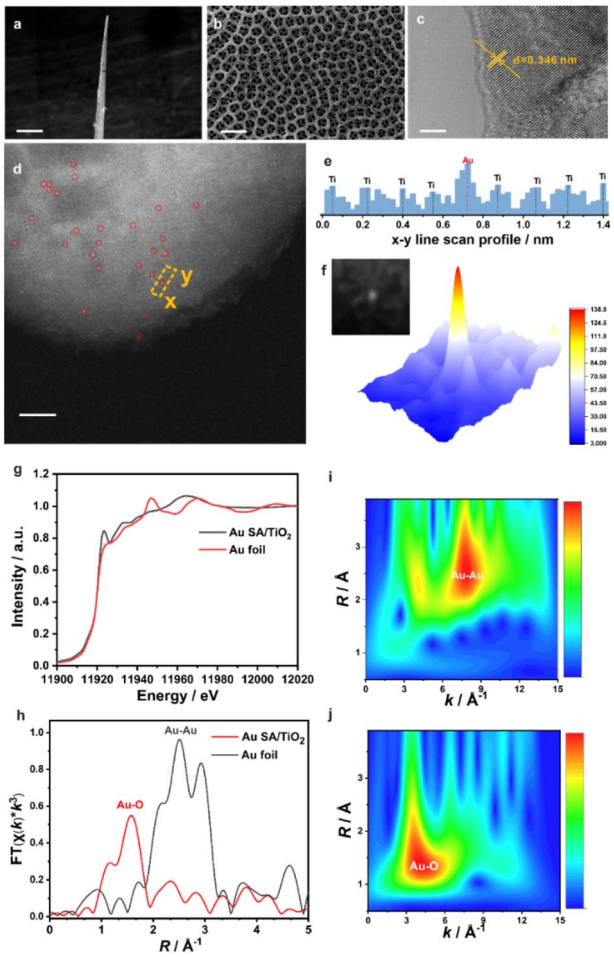

Fig. 2 (a) Overall morphology of the Ti wire-based photoelectrode, the scale bar is 100 μm; (b) top-view SEM image of Au SA/TiO_2, the scale bar is 200 nm; (c) HRTEM image of Au SA/TiO_2, the scale bar is 5 nm; (d) AC HAADF-STEM image of Au SA/TiO_2, the scale bar is 5 nm; (e) line profiles of AC HAADF-STEM image and structural model of a single Au site; (f) 3D heatmap of the brightness of the enlarged AC HAADF-STEM image of Au SA; (g) L_3-edge XANES spectra of Au SA/TiO_2 with Au foil as the reference; (h) Fourier-transformed k^3-weighted EXAFS spectra of Au SA/TiO_2 and Au foil; wavelet transform for k^3-weighted EXAFS spectra of (i) Au foil and (j) Au SA/TiO_2.

XPS analysis (Fig. S6 in the ESI†) shows a negative shift in O 1s binding energy for Au SA/TiO_2 compared to TiO_2 and Au NP/TiO_2, suggesting electron transfer between Au SA and O in TiO_2. Valence band XPS spectra (Fig. S7 in the ESI†) show band edges at 2.89 eV (TiO_2) and 2.65 eV (Au SA/TiO_2), and band tails at 1.85 eV (TiO_2) and 1.35 eV (Au SA/TiO_2). These values illustrate the energy band structures (Fig. S8 in the ESI†), with Au SA/TiO_2 exhibiting a narrowed band gap and lifted valence band position for efficient PEC performance. ICP-OES evaluates Au SA amount, which can be modulated during cryo-electrodeposition (Fig. S9a in the ESI†), while Au NP amount is controlled by sputtering time (Fig. S9b in the ESI†).

The specific aptamers of DA were modified with thiol groups at their 5′ ends, allowing them to be immobilized on the Au SA and Au NP surface through Au–S bonds. To characterize the successful modification of the aptamers, HAADF-STEM images and the corresponding energy dispersive X-ray spectroscopy (EDS) elemental mapping images of aptamer/Au SA/TiO_2 and aptamer/Au NP/TiO_2 are presented in Fig. S10a and b in the ESI† respectively. Different from aptamer/Au NP/TiO_2, where distinct Au NPs can be detected, the aptamer/Au NP/TiO_2 did not show any aggregated nanoparticles except the TiO_2 nanotube structure. Notably, the straightforward representation of aptamers was depicted through S elemental mapping images. The presented results suggested that the aptamers on Au SA indicated a single molecular dispersion. In contrast, on the Au NPs, the Au and S elements exhibited an exactly consistent spatial distribution, indicating that the aggregation of Au NPs induced the aggregation of the aptamers (Fig. S11 in the ESI†). Meanwhile, density functional theory (DFT) calculations were conducted to verify the connection between Au and S atoms. As depicted in Fig. S12a in the ESI,† the TiO_2 substrate with an Au single atom and a thiol chain exhibited an adsorption energy of −2.4734 eV. However, when the second thiol group was introduced, as shown in Fig. S12b in the ESI,† the adsorption energy increased significantly with the value of 2.3232 eV. This shift from negative to positive adsorption has proved that a gold single atom on the TiO_2 substrate can only connect one thiol group. Consequently, an aptamer can attach to only one gold atom, confirming the specificity of the interaction between the gold atom and the thiol group.

The aptamer/Au SA/TiO_2 and aptamer/Au NP/TiO_2 were utilized as PEC aptasensors for evaluation of selectivity for DA detection. Catecholamines, NE, EP, and 5-HT, with similar chemical structures to DA, were selected as interferences. Besides catecholamines, analogues such as tyrosine (Tyr), levodopa (L-DOPA), 3,4-dihydroxyphenylacetic acid (DOPAC) and carbidopa, and other neurotransmitters such as glutamic acid (Glu), γ-aminobutyric acid (GABA) and acetyl choline (Ach) were also taken as interferences. As presented in Fig. 3a, aptamer/Au SA/TiO_2 showed a distinctively high selectivity for DA response, while aptamer/Au NP/TiO_2 (Fig. 3b) did not exhibit selective response characteristics towards DA, as multiple structurally similar molecules elicited distinct response signals on aptamer/Au NP/TiO_2, indicating its poor selectivity for DA, which can be attributed to the recognition failure of intermolecular forces caused by the bush-like structure formed by the reciprocal cross-linking of aptamers on Au NPs. Therefore, the single molecular distribution of the aptamer on the Au single atom site contributed high selectivity for DA detection. The corresponding selectivity of DA with different gold contents is shown in Fig. S13 in the ESI† with the photocurrent response charge ratios of DA/NE. It is worth nothing that we have also optimized the aptamer binding density for aptamer/Au NP/TiO_2 sensors by adjusting the concentration of DA aptamers (Fig. S14 in the ESI†). Unfortunately, neither increasing nor decreasing the aptamer incubation concentration (from 0.1 to 3.0 μM) improved the selectivity effectively. The Au single atom with a weight ratio of 0.24% on TiO_2 showed the highest selectivity. Additionally, we quantitatively validated the electrodes' capability to detect 10 nM DA under physiologically relevant conditions (200 μM ascorbic acid, AA), demonstrating robust

© 2025 The Author(s). Published by the Royal Society of Chemistry

Open Access Article. Published on 21 April 2025. Downloaded on 2/20/2026 6:43:14 PM. This article is licensed under a Creative Commons Attribution-NonCommercial 3.0 Unported Licence.

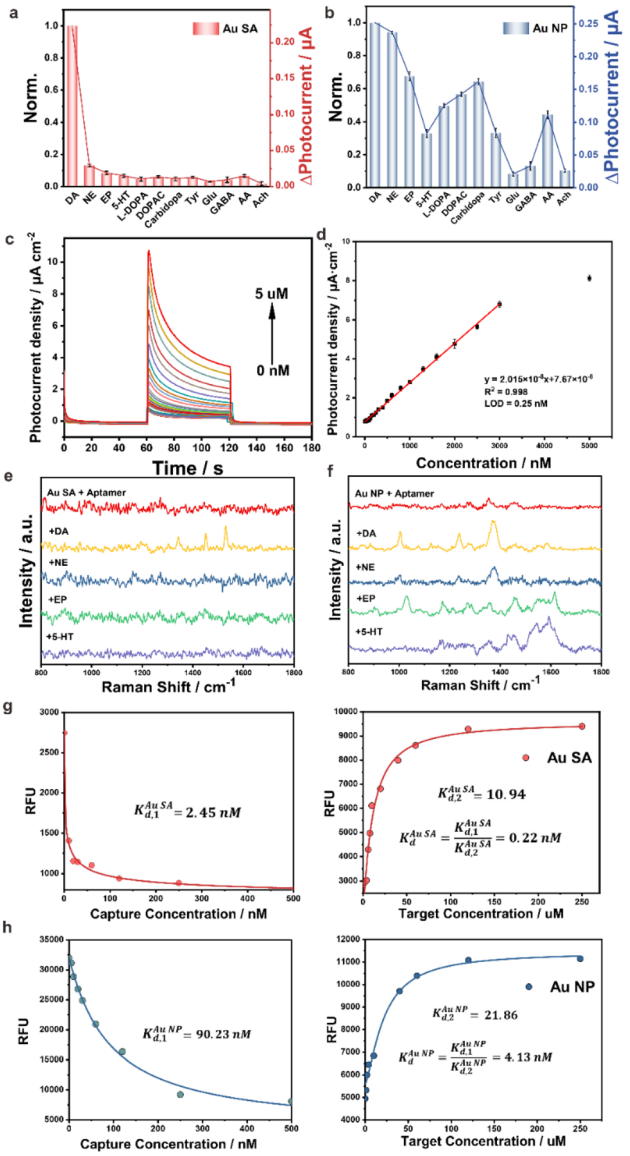

Fig. 3 Selective PEC detection of DA (100 nM) on (a) aptamer/Au SA/TiO_2 and (b) aptamer/Au NP/TiO_2 with interferences of NE, EP and 5-HT with the concentration of 100 nM, L-DOPA, DOPAC, carbidopa, Tyr, Glu, GABA, AA and Ach with the concentration of 1 μM; aptamer/Au SA/TiO_2 PEC plots (c) and its linear calibration curve (d) for DA detection in PBS; Raman spectra of (e) aptamer/Au SA/TiO_2 and (f) aptamer/Au NP/TiO_2 without/with DA, NE, EP, and 5-HT exposure; fluorescence–concentration curves for the K_d constant of DA on (g) aptamer/Au SA/TiO_2 and (h) aptamer/Au NP/TiO_2.

selectivity even in this challenging interference-rich environment (Fig. S15 in the ESI†). As depicted in Fig. 3c, the aptamer/Au SA/TiO_2 reached a linearity from 2 nM to 3 μM of DA with a low detection limit of 0.25 nM (Fig. 3d) in PBS. A similar experiment was also performed in aCSF (Fig. S16 in the ESI†). Meanwhile, the photoelectrode showed excellent reproductivity and repeatability (Fig. S17 in the ESI†). We have conducted a comparative analysis of the performance of our aptamer/Au SA/TiO_2 electrode with other highly selective DA sensors reported in the literature (Table S2 in the ESI†). This comparison includes metrics such as selectivity, sensitivity, and *in vivo* stability. The table highlights how our aptamer/Au SA/TiO_2 electrode performs relative to other state-of-the-art sensors in terms of these critical parameters.

To experimentally validate the selective capture property of the aptamer on Au SA and Au NPs, Raman spectra were employed to characterize the unique absorptions of DA and its analogues. As shown in Fig. 3e, for aptamer/Au SA/TiO_2, no obvious Raman peak can be detected, while after exposing the aptasensor to DA solution, featured Raman peaks can be detected. However, on exposing the aptasensor to NE, EP, and 5-HT, no distinct Raman peaks were observed. These results indicated that the aptamer on Au SA just adsorbed DA and thus achieved excellent selectivity, which was unlike aptamer/Au NP/TiO_2 as exposing to solutions of DA, NE, EP, and 5-HT, each chemical exhibited specific Raman peaks (Fig. 3f), indicating that the above molecules were adsorbed by aptamers on Au NPs, and thus resulted in poor selectivity. Furthermore, fluorescence assays were used as well to numerically characterize aptamer–target dissociation constants (K_d) to further validate the cause of selectivity difference in terms of molecular forces. The K_d was determined by employing nonlinear least-squares fitting to the Hill equation (eqn (1)), with the Hill coefficients (n) designated as a variable.[33]

$$S = S_i + (S_f - S_i)\frac{[T]^n}{[K_d]^n + [T]^n} \quad (1)$$

where S represents the fluorescence signal as a function of $[T]$. The terms S_i and S_f refer to the initial and final signals, respectively. K_d signifies the effective dissociation constant of the complex of interest. Following the completion of titration experiments, the intensities of fluorescence were subjected to a fit according to the Hill equation. The aptamer–competitor strategy was used to extract K_d. In short, a DNA competitor (capture) complementary to the aptamer (sensor) could be displaced by DA (target). Au nanoparticles with the size of 13 nm were used and their UV-vis spectra are shown in Fig. S18 in the ESI.† Notably, the sensor was modified with fluorescein at the 5′ ends and the capture was modified with dabcyl at their 3′ ends. $K_{d,1}$ (eqn (2)) represents the equilibrium between the sensor and competitor. Since Förster resonance energy transfer occurred between the sensor and capture, fluorescence was gradually quenched with the addition of the capture. As the DA target displaced the capture strand from the sensor, the strand reannealed, facilitating DA binding to the sensor and resulting in increased fluorescence, which was defined as the equilibrium (eqn (3)). Based on $K_{d,1}$ and $K_{d,2}$ values, the overall process of K_d could be calculated (eqn (4)) with values of 0.22 nM (Fig. 3g) and 4.13 nM (Fig. 3h) for aptamer/Au SA/TiO_2 and aptamer/Au NP/TiO_2 respectively. The relatively smaller K_d values on aptamer/Au SA/TiO_2 indicated that, compared to Au NPs, Au SA anchored single-molecule aptamers indeed exhibited better selectivity for DA.

$$K_{d,1} = \frac{[\text{Sensor}][\text{Capture}]}{[\text{Sensor–Capture complex}]} \quad (2)$$

Open Access Article. Published on 21 April 2025. Downloaded on 2/20/2026 6:43:14 PM. This article is licensed under a Creative Commons Attribution-NonCommercial 3.0 Unported Licence.

$$K_{d,2} = \frac{[\text{Capture}][\text{Sensor–Target complex}]}{[\text{Sensor–Capture complex}][\text{Sensor}]} \quad (3)$$

$$K_d = \frac{[\text{Sensor}][\text{Target}]}{[\text{Sensor–Target complex}]} = \frac{K_{d,1}}{K_{d,2}} \quad (4)$$

Though the aptamer/Au SA/TiO_2 aptasensor showed better selectivity for DA detection than the aptamer/Au NP/TiO_2 aptasensor, the impact of photoelectron transfer by single-molecule-level dispersed aptamers as opposed to interlinked aptamer nano-bushes was further investigated in detail, thereby ensuring that the aptasensors not only achieved highly selective detection but also had excellent detection sensitivity. The photocurrent responses on Au SA/TiO_2 and Au NP/TiO_2 and corresponding aptasensors were evaluated and are presented in Fig. 4a and b respectively. For Au SA/TiO_2, after bonding with the aptamer, the photocurrent further increased, which indicated that the single molecular dispersed aptamer provided a simple charge transfer channel, and thus facilitated the charge separation. However, for Au NP/TiO_2, after bonding with aptamers, the photocurrent significantly decreased, which implied that the interlinked aptamers induced complex charge transport channels, and thus hampered efficient charge transfer.

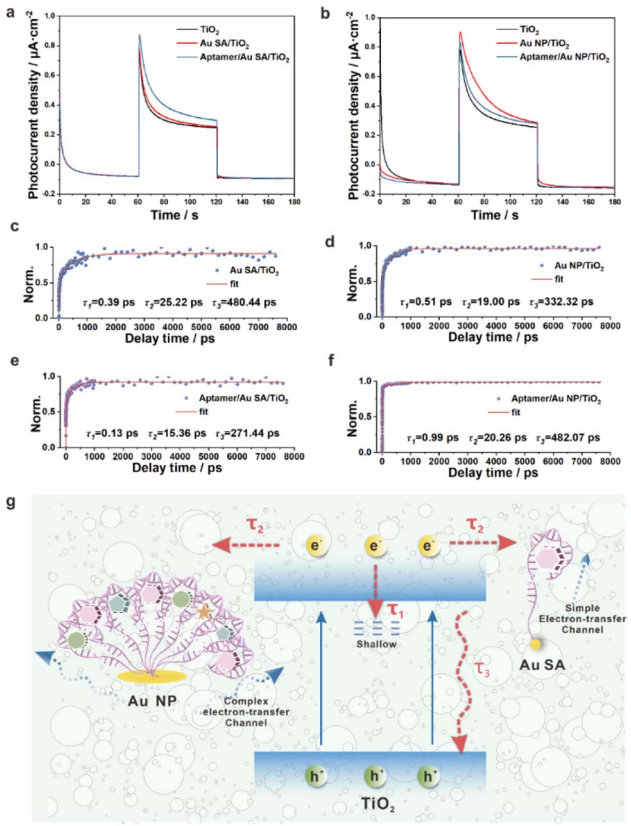

Fig. 4 Photocurrent responses on (a) TiO_2, Au SA/TiO_2, and aptamer/Au SA/TiO_2, and (b) TiO_2, Au NP/TiO_2, and aptamer/Au NP/TiO_2 photoelectrodes under illumination of NIR light; fs-TAS kinetics curves of (c) Au SA/TiO_2, (d) Au NP/TiO_2, (e) aptamer/Au SA/TiO_2, and (f) aptamer/Au NP/TiO_2; (g) schematic representation of the proposed charge trapping model on aptamer/Au NP/TiO_2 and aptamer/Au SA/TiO_2.

Similar PEC responses on Au SA/TiO_2 and Au NP/TiO_2 aptasensors were recorded from incident-photon-current-conversion efficiency (IPCE) spectra (Fig. S19 in the ESI†), electrochemical impedance spectra (Fig. S20 in the ESI†), Mott–Schottky plots (Fig. S21 in the ESI†), and open circuit photovoltage decay curves (Fig. S22 in the ESI†). Compared with Au SA/TiO_2, after bonding with the aptamer, the aptamer/Au SA/TiO_2 presented higher PEC response in the NIR light region, lower impedance, higher carrier density, and longer charge lifetime. However, the aptamer/Au NP/TiO_2 system presented diametrically opposite consequences.

To further investigate the intrinsic mechanism of electron transfer after bonding the aptamer on Au SA and Au NPs, a powerful time-resolved technique of femtosecond transient absorption spectroscopy (fs-TAS) for tracking of photogenerated carrier charge transfer dynamics was employed with a pumping laser of 350 nm and probing wavelength of 540 nm. As shown in Fig. 4c–f, the transient absorption spectra of four samples of Au SA/TiO_2, Au NP/TiO_2, aptamer/Au SA/TiO_2, and aptamer/Au NP/TiO_2 were well fitted by a tri-exponential function with corresponding recovery kinetics.[34,35] These three-decay kinetics were respectively attributed to electron transfer to a shallow trapping state (τ_1), to Au SA or Au NPs (τ_2), to recombine with holes (τ_3) (Fig. 4g). For Au SA/TiO_2, after binding with the aptamer, both τ_2 and τ_3 values decreased, which indicated that the simple electron-transfer channel between Au SA and single molecular aptamer further accelerated electron movement, while for Au NP/TiO_2, after binding with aptamers, both τ_2 and τ_3 values increased, which revealed that the complex electron-transfer channel between Au NPs and aptamers lowered the electron mobility. To further comprehend the intrinsic meaning of τ_2, namely the electron transfer between Au SA and Au NPs, DFT calculations were carried out. The yellow part symbolizes the local electron accumulation area and the cyan part symbolizes the local electron depletion area respectively. By comparing the local charge density difference of Au SA/TiO_2 (Fig. S23 in the ESI†) and Au NP/TiO_2 (Fig. S24a in the ESI†), after bonding with one thiol bond, stronger charge transfer activity between Au SA and TiO_2 sites was observed. On this basis, the other thiol bond was introduced to the Au NPs/TiO_2 (Fig. S24b in the ESI†). It was pretty obvious that the greater charge between Au NPs/TiO_2 by adding –SH resulted in a lesser charge accumulation region located in Au and TiO_2. That means, in the presence of Au NPs, the more thiol bonds the system had, the more difficult the charge transfer from TiO_2 to Au NPs, which explained the reason for the change of τ_2 from another aspect.

For practical *in vivo* DA detection, the PEC aptasensor was further modified with an anti-biofouling hydrogel layer to block the biological contamination, such as proteins, tissues, and cells (Fig. S25 in the ESI†). The anti-biofouling performance of Gel/aptasensor was evaluated from SEM images (Fig. S26 in the ESI†), contamination degree of fluorescein isothiocyanate-labelled protein (Fig. S27 in the ESI†), static water contact angle measurements (Fig. S28 in the ESI†), and electrochemical characterization (Fig. S29 in the ESI†). The hydrogel layer with

© 2025 The Author(s). Published by the Royal Society of Chemistry

Open Access Article. Published on 21 April 2025. Downloaded on 2/20/2026 6:43:14 PM.
This article is licensed under a Creative Commons Attribution-NonCommercial 3.0 Unported Licence.

high hydrophilicity and suitable nanoporous structures demonstrated excellent anti-biofouling properties, but did not have any impact on the detection of small molecules of DA (Fig. S30 in the ESI†) and the linear range (Fig. S31 in the ESI†). The photocurrent response of Gel/aptasensor is remarkably rapid, achieving equilibrium within 4.7 seconds (Fig. S32 in the ESI†), and it exhibits negligible change after immersing in artificial cerebrospinal fluid (aCSF) containing 20 mg mL^{-1} bovine serum albumin (BSA) (Fig. S33 in the ESI†). Similarly, the PEC performances of Gel/aptasensor before and after the *in vivo* experiment showed little change (Fig. S34 in the ESI†). The photocurrent signal with Gel/aptasensor in the striatum of mice after injecting with saline (0.9%) for 30 minutes was quite stable and presented insignificant changes (Fig. S35 in the ESI†).

The practical applicability of the aptamer/Au SA/TiO_2 micro-photoelectrode for detecting DA levels in the brains of living mice has been evaluated, as schematically presented in Fig. 5a. In a representative experiment, the micro-photoelectrode was implanted in the striatum, a brain area replete with DA vesicles, of a C57BL/6 mice brain subjected to anesthesia. Nomifensine, a selective DA reuptake inhibitor that elevates DA levels, was first injected intraperitoneally (Fig. 5b).[36] Following this, α-methyl-DL-tyrosine methyl ester hydrochloride (αMPT), which lowers extracellular DA levels by inhibiting its synthesis,[37] was infused intraperitoneally once the DA levels stabilized (Fig. 5c). The micro-photoelectrodes adeptly detected the signals corresponding to the DA level changes induced by both agents. To validate the PEC findings, immunofluorescence analysis was performed (Fig. 5d), revealing an increase in fluorescence intensity post-nomifensine injection and a subsequent decrease after αMPT infusion, aligning with the anticipated results.

To further verify the practicability of the aptamer/Au SA/TiO_2 micro-photoelectrode, a typical acute Parkinson's disease (PD) model was created through administering 1-methyl-4-phenyl-1,2,3,6-tetrahydropyridine (MPTP) with the dose of 20 mg kg^{-1} for four times.[38,39] PD is a neurodegenerative disorder characterized by the degeneration of nigrostriatal DA neurons and striatal DA depletion, with primary symptoms including bradykinesia, akinesia, and rigidity.[28,40,41] We compared the immunohistochemical staining of tyrosine hydroxylase (TH) positive density between normal and PD mice to verify the PD model (Fig. 5e). As the rate-limiting enzyme for the synthesis of DA precursors, the TH-positive density in the substantia nigra (SN) of the PD mice section (Fig. 5f) was lower than that of the normal mice, indicating a reduction of dopaminergic neurons in the PD model. In addition, the typical open field test was then conducted to verify the PD model's motor ability (Fig. 5g). The motion tracks clearly demonstrated that the PD mouse was less active compared to the normal ones (Fig. 5h). Therefore, both physiological and behavioural experimental results confirmed the successful establishment of the PD model. Furthermore, high-K^+ stimulation was employed as a model system to evaluate the performance of DA release from the striatum of living mice brains. The photocurrent response following high-K^+ stimulation demonstrated that the response in PD mice was significantly diminished compared to that of normal mice

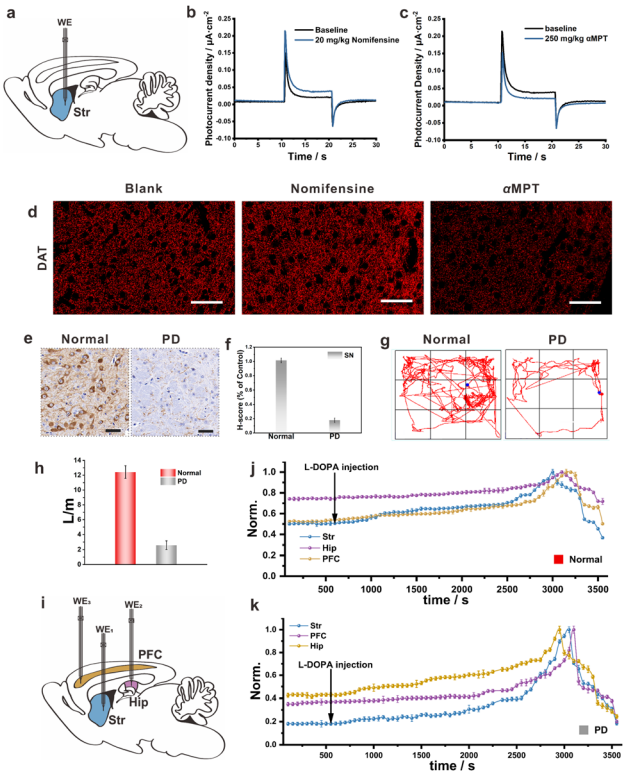

Fig. 5 (a) Schematic illustration of the aptamer/Au SA/TiO_2 micro-photoelectrode for *in vivo* DA detection in the striatum; PEC response of the aptamer/Au SA/TiO_2 micro-photoelectrode in the striatum of mice subjected to anesthesia stimulated by the injection of (b) nomifensine (20 mg kg^{-1}, i. p.) and (c) αMPT (250 mg kg^{-1}, i. p.); (d) immunofluorescence analysis of the brain sections in Str, stained with anti-DAT antibody in the blank sample, and after injection of nomifensine and αMPT samples, the scale bar is 20 μm; (e) immunohistochemical staining of TH in the SN of normal (left) and PD (right) mice, and corresponding quantitative analysis of normal and PD mice (f) (n = 4 mice, ***$p < 0.001$); (g) open field test for typical motion tracks of the normal (left) and the PD (right) mice in 5 min in an empty arena and (h) relative total distance, the significance was determined by two-tailed unpaired Student's t-test (n = 4 mice, ***$p < 0.001$); (i) schematic illustration of aptamer/Au SA/TiO_2 micro-photoelectrodes in three brain regions for simultaneously monitoring DA; (j) normalized plots for variations of the DA concentration in the striatum, hippocampus, and prefrontal cortex of (j) normal and (k) PD mice brains after 100 mg kg^{-1} dose of L-Dopa injection for long time monitoring. The above-mentioned data are all presented as mean ± S.D. Error bars: S.D (n = 4 mice).

(Fig. S36 in the ESI†), further substantiating the deficit in dopaminergic neurons.

Furthermore, the aptamer/Au SA/TiO_2 micro-photoelectrode was utilized for monitoring across multiple brain regions. As illustrated in Fig. 5i, three working electrodes were respectively implanted into the striatum (Str), hippocampus (Hip), and prefrontal cortex (PFC). Following this, we compared the changes between normal (Fig. 5j) and PD (Fig. 5k) mice after administering L-DOPA. L-DOPA, a precursor to DA, can elevate DA levels and is thus widely used in PD treatment. After implanting the micro-photoelectrodes for 10 minutes, L-DOPA was injected. It was evident that both normal and PD mice

Open Access Article. Published on 21 April 2025. Downloaded on 2/20/2026 6:43:14 PM. This article is licensed under a Creative Commons Attribution-NonCommercial 3.0 Unported Licence.

exhibited a gradual increase in DA levels, reaching a peak within the next 30 minutes. From the normalized data, it was observed that PD mice appeared more responsive to L-DOPA than normal mice. This increased sensitivity in PD mice was attributed to the severe depletion of DA, necessitating a greater amount of L-DOPA to produce supplementary DA. In contrast, the injection of L-DOPA in normal mice only marginally increased DA levels above the baseline. Our findings confirmed that the photoelectrodes could support a period of time monitoring across multiple brain regions.

To further demonstrate the superior selectivity of aptamer/Au SA/TiO_2 micro-photoelectrodes and to implement quantitative DA *in vivo* detection, four micro-photoelectrodes were implanted into cingulum (Cg), Str, Hip, and PFC, respectively (schematics in Fig. 6a). The Cg, a brain region without DA,[42,43] was used as a referenced *in vivo* environment for calibration with the *in vitro* measurements (Fig. S37 in the ESI†), facilitating dynamic monitoring of DA fluctuations rather than absolute quantification by leveraging the stable background (*i.e.*, AA) to detect transient DA changes induced by physiological stimuli. The quantitative *in vivo* DA detection in Str, Hip, and PFC of normal and PD mice is plotted in Fig. 6b, c and d, respectively. In all three brain regions, the aptamer/Au NP/TiO_2 showed stronger photocurrent intensity than aptamer/Au SA/TiO_2 both for normal and PD mice, which indicated that the aptamer/Au NP/TiO_2 not only captured DA, but also trapped analogue neurotransmitters, such as NE, EP, and 5-HT. By comparing the selective DA responses on aptamer/Au SA/TiO_2 in three brain regions between PD and normal mice, we revealed that the onset of PD caused by MPTP appeared to be solely related to the depletion of DA in Str, while having little effect on DA in Hip and PFC. Notably, compared with normal mice, the signal intensity in PFC showed a distinct decrease on aptamer/Au NP/TiO_2 for PD mice, while the signal was maintained in a steady state on aptamer/Au SA/TiO_2, which revealed a conclusion different from the previously reported results.[44,45] During the occurrence of PD, in the PFC region, the concentration of DA did not show a significant decrease, while, the obvious signal decline on aptamer/Au NP/TiO_2 should be attributed to the reduction of other neurotransmitters. That is, the high DA selectivity on aptamer/Au SA/TiO_2 uncovered the subdivided functions of neurotransmitters, which are further validated in the following biochemical analysis.

To verify the conclusion drawn from PEC detection, histology causes were first investigated. Hematoxylin–eosin (HE) staining of the Hip and PFC in both normal and PD mice is shown in Fig. S38 in the ESI.† The Hip region appeared well-organized with healthy cell statuses and distinct boundaries, and the neurons in the PFC region of normal mice were densely arranged, exhibiting uniform cell morphology with clear nucleoli. Conversely, PD neurons displayed irregular shapes and smaller neuronal cell bodies. Subsequently, immunohistochemistry was employed to assess tyrosine hydroxylase (TH) levels in the Str, Hip, and PFC (Fig. 6e). TH, being the rate-limiting enzyme for dopamine (DA) and norepinephrine (NE), reflected the levels of DA and NE.[46–48] It was observed that, post-PD, TH levels in the Str significantly decreased (Fig. 6f), which

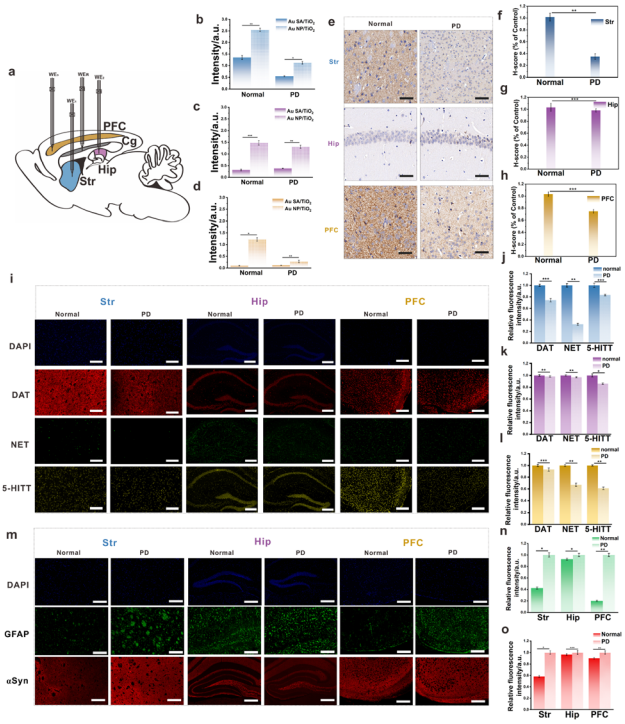

Fig. 6 (a) Schematic illustration of aptamer/Au SA/TiO_2 micro-photoelectrodes in four multiple brain regions of Cg, Str, Hip, and PFC; photocurrent signals on aptamer/Au SA/TiO_2 and aptamer/Au NP/TiO_2 micro-photoelectrodes in (b) Str, (c) Hip, and (d) PFC of normal and PD mice ($n = 4$ electrodes); (e) immunohistochemical staining of TH in the brain regions and corresponding quantitative analysis in (f) Str, (g) Hip, and (h) PFC, the scale bar is 50 μm ($n = 4$ mice); (i) co-immunoreactivity analysis of the brain sections from the normal and the PD mice by immunofluorescence, stained with anti-DAT antibody (red), anti-NET antibody (green), and anti-5-HITT antibody (yellow), the scale bars are 20 μm; the corresponding quantitative analysis of relative fluorescence intensity in the region of (j) Str, (k) Hip, and (l) PFC; (m) immunofluorescence analysis of the brain sections in Str, Hip, and PFC, stained with GFAP antibody (green) and αsyn antibody (red), the scale bars are 100 μm, and the corresponding quantitative results expressed as the relative fluorescence intensity of (n) GFAP and (o) αSyn ($n = 4$ mice). The data are all expressed as mean ± SD. Significance was determined by two-tailed unpaired Student's *t*-test (*$p < 0.05$, **$p < 0.01$, ***$p < 0.001$).

was a hallmark of PD. Conversely, TH levels in the Hip remained largely unchanged (Fig. 6g). Notably, a slight reduction occurred in the PFC (Fig. 6h), potentially associated with decreased NE levels.[49]

The distribution of various neurotransmitters, identified by their respective translocators, was discernible through combined immunofluorescence. Results are shown in Fig. 6i, with corresponding quantitative analysis of relative fluorescence intensity in Fig. 6j–l. The differences between normal and PD conditions aligned well with the PEC results, indicating a sharp decline in the Str and minimal changes in the PFC and Hip. Meanwhile, all three translocators exhibited declines in the Str of PD mice, with no variations in the Hip. Interestingly, the expressions of both norepinephrine transporter (NET) and serotonin transporter (5-HITT) in the PFC decreased in PD, but

© 2025 The Author(s). Published by the Royal Society of Chemistry

Open Access Article. Published on 21 April 2025. Downloaded on 2/20/2026 6:43:14 PM. This article is licensed under a Creative Commons Attribution-NonCommercial 3.0 Unported Licence.

5-HITT showed a more pronounced reduction. These findings indicated that the differential PEC responses between Au SA and Au NPs in the PFC primarily resulted from decreases in NE and serotonin (5-HT), while Au NPs' low selectivity caused simultaneous capture of DA analogues, consequently resulting in a marked change in Au NP responses between normal and PD mice.

Glial fibrillary acidic protein (GFAP), a marker of astrocyte activation, is linked to damage in the central nervous system, making elevated GFAP levels in tissues a signature response to such damage.[50] Meanwhile, the accumulation of alpha-synuclein (αSyn) amyloid fibrils is a primary pathological indicator of PD,[51,52] thus increased αSyn expression is often regarded as a manifestation of oxidative stress in the PD brain (Fig. 6m). As depicted in Fig. 6n, GFAP expression in the Str and PFC experienced a notable increase post-PD, while remaining unchanged in the Hip. However, regarding αSyn, only the Str exhibited a significant upsurge after PD onset, with minor elevations in both Hip and PFC (Fig. 6o). This alteration in αSyn suggested that MPTP scarcely inflicted damage in the Hip, explaining why neurotransmitter levels remain stable there. In contrast, MPTP moderately affected the PFC, leading to modifications in neurotransmitters other than DA, given the absence of substantial αSyn aggregation. Undeniably, increases in both GFAP and αSyn in the Str can be attributed to the downturn in all neurotransmitters. To further verify our neurotransmitter dynamic pattern, high-performance liquid chromatography with a fluorescence detector (HPLC/FLD) was constructed to measure dopamine concentration. As followed in Table S3 in the ESI,† it was clear that after the Parkinson's disease (PD), the level of DA, especially in the striatum, dramatically decreased, which could confirm the huge depletion of DA in PD. As a contrast, there is only a slight decrease of the level of DA in the other two brain regions, showing almost constant values. The above results could confirm our conjecture from another aspect.

Meanwhile, behavioural experiments were conducted to further verify the above results. Previous lesion studies have highlighted the crucial role of the medial PFC in temporal order recognition (TOR) memory.[53] There was no significant difference in the discrimination ratio between normal mice and PD mice (Fig. S39 in the ESI†), suggesting that MPTP-induced PD did not impair TOR memory and has no impact on the PFC's recognition function. Concurrently, a new object recognition (NOR) test was employed to assess Hip function. As demonstrated in Fig. S40 in the ESI,† the discrimination ratio of NOR remained virtually unchanged between normal and PD mice, indicating that MPTP-induced PD did not affect NOR memory.

Conclusions

In this study, we introduced a novel photoelectrochemical single molecular aptamer sensor (PEC-sm-aptasensor) based on atomic-level dispersion of aptamers on gold single-atom/titanium dioxide (Au SA/TiO_2) photoelectrodes for highly selective *in vivo* detection of DA in various brain regions of living mice. Our findings not only advance the field of aptasensor technology but also provide new insights into the neurochemistry of PD. Our results significantly contrast with previous studies that suggested a decrease in cortical dopamine levels in PD models. In contrast to these findings, our PEC-sm-aptasensor revealed that while the total concentration of neurotransmitters decreases in PD, the concentration of DA in the prefrontal cortex remains constant. This discovery aligns with recent studies emphasizing the complexity of neurochemical changes in PD and challenges the traditional view of a uniform decrease in DA levels across brain regions. The high selectivity and sensitivity of our PEC-sm-aptasensor allowed for this nuanced understanding, highlighting the importance of advanced detection technologies in neurochemical research. The observed constancy of DA levels in the prefrontal cortex, despite a decrease in other neurotransmitters, suggests that cognitive functions may be less affected in early stages of PD than previously thought. This finding could have significant implications for the development of targeted therapies that aim to preserve the cognitive function in PD patients. The PEC-sm-aptasensor's ability to discern this pattern underscores the role of single molecular-level dispersion in enhancing sensor specificity, allowing for accurate detection in complex biological environments. While our study provides ground-breaking insights, it is not without limitations. The PEC-sm-aptasensor, although highly selective, is designed specifically for DA detection. Expanding its application to other neurotransmitters would require the development of aptamers with similar selectivity. Additionally, the long-term stability of the sensor *in vivo* and its potential for use in human studies remain to be determined. These factors could influence the broader application and interpretation of our results. Future research should focus on expanding the PEC-sm-aptasensor's capabilities to detect a range of neurotransmitters simultaneously. This would provide a more comprehensive picture of neurochemical changes in PD and other neurological disorders. Additionally, investigating the sensor's long-term stability and biocompatibility *in vivo* is crucial for its translational potential. Furthermore, exploring the mechanisms underlying the observed neurochemical patterns could reveal new targets for therapeutic intervention in PD. The development of the PEC-sm-aptasensor has broad implications for the field of neuroscience and neurodegenerative disease research. By enabling highly selective and sensitive *in vivo* detection of neurotransmitters, our work paves the way for more accurate diagnosis, monitoring, and treatment of PD and potentially other neurological disorders. The ability to track neurochemical changes in real-time could also impact the development of personalized medicine strategies, tailoring treatments to individual patients' neurochemical profiles. This study, therefore, not only contributes to the advancement of aptasensor technology but also holds promise for improving clinical outcomes in neurodegenerative diseases.

Ethical statement

All procedures involving animals were conducted with the approval of the Animal Ethics Committee in ECNU, China. Male C57 mice (6–8 weeks old, weight ranges from 18 to 20 g) were

Open Access Article. Published on 21 April 2025. Downloaded on 2/20/2026 6:43:14 PM. This article is licensed under a Creative Commons Attribution-NonCommercial 3.0 Unported Licence.

purchased from Shanghai SLAC Laboratory Animal Co. Ltd. And all surgical procedures involving mice were conducted in accordance with the Guidelines for the Care and use of Laboratory Animals of ECNU.

Data availability

The data supporting this article have been included in the main text and the ESI.†

Author contributions

J. H. and Z. Z. designed the experiments. J. H. and S. G. carried out the synthesis of the photoelectrode and photoelectrochemical measurements. X. Z. and Y. L. performed the morphological and elemental characterization studies. All authors wrote the manuscript.

Conflicts of interest

There are no conflicts to declare.

Acknowledgements

This research was supported by the National Natural Science Foundation of China (No. 22474041).

Notes and references

1 J. Yan, R. Bhadane, M. Ran, X. Ma, Y. Li, D. Zheng, O. M. H. Salo-Ahen and H. Zhang, *Nat. Commun.*, 2024, **15**, 3684.
2 A. D. Ellington and J. W. Szostak, *Nature*, 1990, **346**, 818–822.
3 M. Kimoto, H. P. Tan, K. Matsunaga, N. A. B. M. Mislan, G. Kawai and I. Hirao, *J. Am. Chem. Soc.*, 2023, **145**, 20432–20441.
4 M. R. Dunn, R. M. Jimenez and J. C. Chaput, *Nat. Rev. Chem.*, 2017, **1**, 0076.
5 F. Bottari, E. Daems, A. M. de Vries, P. V. Wielendaele, S. Trashin, R. Blust, F. Sobott, A. Madder, J. C. Martins and K. D. Wael, *J. Am. Chem. Soc.*, 2020, **142**, 19622–19630.
6 I. Willner and M. Zayats, *Angew. Chem., Int. Ed.*, 2007, **46**, 6408–6418.
7 N. Li and C. M. Ho, *J. Am. Chem. Soc.*, 2008, **130**, 2380–2381.
8 W. Q. Zhang, Y. D. Tu, H. Liu, R. Liu, X. J. Zhang, L. Jiang, Y. Huang and F. Xia, *Angew. Chem., Int. Ed.*, 2024, **63**, e202316434.
9 Y. Liu, Z. Liu and Y. Tian, *Acc. Chem. Res.*, 2022, **55**, 2821–2832.
10 B. R. Baker, R. Y. Lai, M. S. Wood, E. H. Doctor, A. J. Heeger and K. W. Plaxco, *J. Am. Chem. Soc.*, 2006, **128**, 3138–3139.
11 X. Zuo, Y. Xiao and K. W. Plaxco, *J. Am. Chem. Soc.*, 2009, **131**, 6944–6945.
12 N. Arroyo-Currás, J. Somerson, P. A. Vieira, K. L. Ploense, T. E. Kippin and K. W. Plaxco, *Proc. Natl. Acad. Sci. U. S. A.*, 2017, **114**, 645–650.
13 J. Gerson, M. K. Erdal, M. H. McDonough, K. L. Ploense, P. Dauphin-Ducharme, K. M. Honeywell, K. K. Leung, N. Arroyo-Curras, J. M. Gibson, N. A. Emmons, W. Meiring, J. P. Hespanha, K. W. Plaxco and T. E. Kippin, *Sci. Adv.*, 2023, **9**, eadg3254.
14 P. Dauphin-Ducharme, K. Yang, N. Arroyo-Currás, K. L. Ploense, Y. Zhang, J. Gerson, M. Kurnik, T. E. Kippin, M. N. Stojanovic and K. W. Plaxco, *ACS Sens.*, 2019, **4**, 2832–2837.
15 N. Nakatsuka, K. A. Yang, J. M. Abendroth, K. M. Cheung, X. Xu, H. Yang, C. Zhao, B. Zhu, Y. S. Rim, Y. Yang, P. S. Weiss, M. N. Stojanović and A. M. Andrews, *Science*, 2018, **362**, 319–324.
16 C. Zhao, K. M. Cheung, I. W. Huang, H. Yang, N. Nakatsuka, W. Liu, Y. Cao, T. Man, P. S. Weiss, H. G. Monbouquette and A. M. Andrews, *Sci. Adv.*, 2021, **7**, eabj7422.
17 J. Ng, A. Papandreou, S. J. Heales and M. A. Kurian, *Nat. Rev. Neurol.*, 2015, **11**, 567–584.
18 M. Perry, Q. Li and R. T. Kennedy, *Anal. Chim. Acta*, 2009, **653**, 1–22.
19 H. Hou, Y. Jin, H. Wei, W. Ji, Y. Xue, J. Hu, M. Zhang, Y. Jiang and L. Mao, *Angew. Chem., Int. Ed.*, 2020, **59**, 18996–19000.
20 A. Stuber, A. Douaki, J. Hengsteler, D. Buckingham, D. Momotenko, D. Garoli and N. Nakatsuka, *ACS Nano*, 2023, **17**, 19168–19179.
21 A. Douaki, A. Stuber, J. Hengsteler, D. Monotenko, D. M. Rogers, W. Rocchia, J. D. Hirst, N. Nakatsuka and D. Garoli, *Chem. Commun.*, 2023, **59**, 14713–14716.
22 Y. Wang, Y. Qian, L. Zhang, Z. Zhang, S. Chen, J. Liu, X. He and Y. Tian, *J. Am. Chem. Soc.*, 2023, **145**, 2118–2126.
23 L. Zhou, R. Yang, X. Li, N. Dong, B. Zhu, J. Wang, X. Lin and B. Su, *J. Am. Chem. Soc.*, 2023, **145**, 23727–23738.
24 F. Sun, J. Zeng, M. Jing, J. Zhou, J. Feng, S. F. Owen, Y. Luo, F. Li, H. Wang, T. Yamaguchi, Z. Yong, Y. Gao, W. Peng, L. Wang, S. Zhang, J. Du, D. Lin, M. Xu, A. C. Kreitzer, G. Cui and Y. Li, *Cell*, 2018, **174**, 481–496.
25 Y. Zhuo, B. Luo, X. Yi, H. Dong, X. Miao, J. Wan, J. T. Williams, M. G. Campbell, R. Cai, T. Qian, F. Li, S. J. Weber, L. Wang, B. Li, Y. Wei, G. Li, H. Wang, Y. Zheng, Y. Zhao, M. E. Wolf, Y. Zhu, M. Watabe-Uchida and Y. Li, *Nat. Methods*, 2024, **21**, 680–691.
26 A. Muller, V. Joseph, P. A. Slesinger and D. Kleinfeld, *Nat. Methods.*, 2014, **11**, 1245–1252.
27 P. Zhang, Z. Tian, Y. Kang, B. He, Z. Zhao, C. T. Hung, L. Duan, W. Chen, Y. Tang, J. Yu, L. Mai, Y. F. Li, W. Li and D. Zhao, *J. Am. Chem. Soc.*, 2022, **144**, 20964–20974.
28 W. Dauer and S. Przedborski, *Neuron*, 2003, **39**, 889–909.
29 F. X. Xiao, Z. Zeng and B. Liu, *J. Am. Chem. Soc.*, 2015, **137**, 10735–10744.
30 X. Chen, L. Liu, P. Y. Yu and S. S. Mao, *Science*, 2011, **331**, 746–750.
31 N. Siemer, A. Lüken, M. Zalibera, J. Frenzel, D. Muñoz-Santiburcio, A. Savitsky, W. Lubitz, M. Muhler, D. Marx and J. Strunk, *J. Am. Chem. Soc.*, 2018, **140**, 18082–18092.
32 J. Wan, W. Chen, C. Jia, L. Zheng, J. Dong, X. Zheng, Y. Wang, W. Yan, C. Chen, Q. Peng, D. Wang and Y. Li, *Adv. Mater.*, 2018, **30**, 1705369.

© 2025 The Author(s). Published by the Royal Society of Chemistry

Open Access Article. Published on 21 April 2025. Downloaded on 2/20/2026 6:43:14 PM.
This article is licensed under a Creative Commons Attribution-NonCommercial 3.0 Unported Licence.

33 J. Hu and C. J. Easley, *Analyst*, 2011, **136**, 3461.
34 X. Fang, Q. Shang, Y. Wang, L. Jiao, T. Yao, Y. Li, Q. Zhang, Y. Luo and H. L. Jiang, *Adv. Mater.*, 2018, **30**, 1705112.
35 X. Xiao, Y. Gao, L. Zhang, J. Zhang, Q. Zhang, Q. Li, H. Bao, J. Zhou, S. Miao, N. Chen, J. Wang, B. Jiang, C. Tian and H. Fu, *Adv. Mater.*, 2020, **32**, 2003082.
36 E. C. P. Hennings, J. P. Kiss, K. De Oliveira, P. T. Toth and E. S. Vizi, *J. Neurochem.*, 1999, **73**, 1043–1050.
37 M. Laruelle, C. D. D'Souza, R. M. Baldwin, A. Abi-Dargham, S. J. Kanes, C. L. Fingado, J. P. Seibyl, S. S. Zoghbi, M. B. Bowers, P. Jatlow, D. S. Charney and R. B. Innis, *Neuropsychopharmacology*, 1997, **17**, 162–174.
38 H. Kuroiwa, H. Yokoyama, H. Kimoto, H. Kato and T. Araki, *Metab. Brain Dis.*, 2010, **25**, 177–183.
39 V. Jackson-Lewis and S. Przedborski, *Nat. Protoc.*, 2007, **2**, 141–151.
40 W. Poewe, K. Seppi, C. M. Tanner, G. M. Halliday, P. Brundin, J. Volkmann, A. E. Schrag and A. E. Lang, *Nat. Rev. Dis. Primers*, 2017, **3**, 17013.
41 M. Coelho and J. J. Ferreira, *Nat. Rev. Neurol.*, 2012, **8**, 435–442.
42 M. O. Klein, D. S. Battagello, A. R. Cardoso, D. N. Hauser, J. C. Bittencourt and R. G. Correa, *Cell. Mol. Neurobiol.*, 2019, **39**, 31–59.
43 E. J. Bubb, C. Metzler-Baddeley and J. P. Aggleton, *Neurosci. Biobehav. Rev.*, 2018, **92**, 104–127.
44 S. Narayanan, R. L. Rodnitzky and E. Y. Uc, *Rev. Neurosci.*, 2013, **24**, 267–278.
45 R. Yang, S. Ye, S. Zhang, H. Huang, Y. Zhang, Y. Yang, S. Xie, L. He, Y. Yang and J. Shi, *NeuroReport*, 2023, **34**, 551–559.
46 C. Hao, A. Qu, L. Xu, M. Sun, H. Zhang, C. Xu and H. Kuang, *J. Am. Chem. Soc.*, 2019, **141**, 1091–1099.
47 S. C. Daubner, T. Le and S. Wang, *Arch. Biochem. Biophys.*, 2011, **508**, 1–12.
48 D. J. Surmeier, J. A. Obeso and G. M. Halliday, *Nat. Rev. Neurosci.*, 2017, **18**, 101–113.
49 K. K. Andersson, D. D. Cox, L. Que, T. Flatmark and J. Haavik, *J. Biol. Chem.*, 1988, **263**, 18621–18626.
50 H. Liu, Y. Han, T. Wang, H. Zhang, Q. Xu, J. Yuan and Z. Li, *J. Am. Chem. Soc.*, 2020, **142**, 21730–21742.
51 M. Lundblad, M. Decressac, B. Mattsson and A. Björklund, *Proc. Natl. Acad. Sci. U. S. A.*, 2012, **109**, 3213–3219.
52 W. Sheehan, C. J. Nadarajah, M. F. Kanan, J. N. Patterson, B. Novotny, J. H. Lawrence, M. W. King, L. Brase, C. E. Inman, C. M. Yuede, J. Lee, T. K. Patel, O. Harari, B. A. Benitez, A. A. Davis and E. S. Musiek, *Neuron*, 2023, **111**, 2383–2398.
53 E. Y. Yuen, J. Wei, W. Liu, P. Zhong, X. Li and Z. Yan, *Neuron*, 2012, **73**, 962–977.